LANGMUIR Article
Cite This: Langmuir 2019, 35, 9274–9285
pubs.acs.org/Langmuir

Deck the Walls with Anisotropic Colloids in Nematic Liquid Crystals

Yimin Luo,[†] Tianyi Yao,[‡] Daniel A. Beller,[§] Francesca Serra,[∥] and Kathleen J. Stebe*[,‡,⊥]

[†]Department of Chemical and Biomolecular Engineering, University of Delaware, Newark, Delaware 19716, United States
[‡]Department of Chemical and Biomolecular Engineering, University of Pennsylvania, Philadelphia, Pennsylvania 19104, United States
[§]Department of Physics, University of California, Merced, California 95343, United States
[∥]Department of Physics and Astronomy, Johns Hopkins University, Baltimore, Maryland 21218, United States

Supporting Information

ABSTRACT: Nematic liquid crystals (NLCs) offer remarkable opportunities to direct colloids to form complex structures. The elastic energy field that dictates colloid interactions is determined by the NLC director field, which is sensitive to and can be controlled by boundaries including vessel walls and colloid surfaces. By molding the director field via liquid-crystal alignment on these surfaces, elastic energy landscapes can be defined to drive structure formation. We focus on colloids in otherwise defect-free director fields formed near undulating walls. Colloids can be driven along prescribed paths and directed to well-defined docking sites on such wavy boundaries. Colloids that impose strong alignment generate topologically required companion defects. Configurations for homeotropic colloids include a dipolar structure formed by the colloid and its companion hedgehog defect or a quadrupolar structure formed by the colloid and its companion Saturn ring. Adjacent to wavy walls with wavelengths larger than the colloid diameter, spherical particles are attracted to locations along the wall with distortions in the nematic director field that complement those from the colloid. This is the basis of lock-and-key interactions. Here, we study ellipsoidal colloids with homeotropic anchoring near complex undulating walls. The walls impose distortions that decay with distance from the wall to a uniform director in the far field. Ellipsoids form dipolar defect configurations with the colloid's major axis aligned with the far field director. Two distinct quadrupolar defect structures also form, stabilized by confinement; these include the Saturn I configuration with the ellipsoid's major axis aligned with the far field director and the Saturn II configuration with the major axis perpendicular to the far field director. The ellipsoid orientation varies only weakly in bulk and near undulating walls. All configurations are attracted to walls with long, shallow waves. However, for walls with wavelengths that are small compared to the colloid length, Saturn II is repelled, allowing selective docking of aligned objects. Deep, narrow wells prompt the insertion of a vertical ellipsoid. By introducing an opening at the bottom of such a deep well, we study colloids within pores that connect two domains. Ellipsoids with different aspect ratios find different equilibrium positions. An ellipsoid of the right dimension and aspect ratio can plug the pore, creating a class of 2D selective membranes.

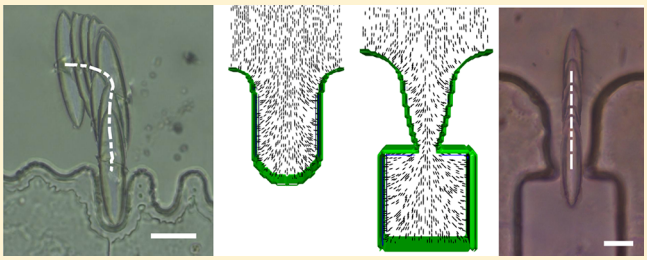

INTRODUCTION

This article is an invited contribution in response to Kathleen Stebe having been one of two Langmuir lecturers in 2018. Her lecture focused on our work on colloid interactions with complex boundaries in nematic liquid crystals. Rather than writing a review article, we present here original work on anisotropic colloids in this field. These results show the promise of the approach that we are developing for control over the colloidal particle position, orientation, and path via elastic energies in nematics via colloid−boundary interactions. To place this work in context, we first review work on spherical colloids in confined nematic liquid crystals (NLCs).

Colloids embedded in NLCs elicit elastic responses, mediated by the NLC director field defined by the shape of bounding surfaces including colloids and vessel walls. These interactions can be used to direct colloid assembly into complex, responsive structures. When placed in NLCs, colloids often form topologically required companion defects.[1] The role of the colloid and companion defect configuration in setting the range and strength of elastic interactions was revealed in pioneering observations of colloidal droplets in NLCs.[2] The field has since burgeoned owing to the richness of the energetic and topological features in these systems.[3] Spherical colloids have been directed to form diverse structures that include linear strings of colloids in dipolar configurations, zigzag strings of colloids in quadrupolar configurations, crystalline structures, and structures with complex topologies guided by laser tweezers,[4,5] to name just a few examples. Particle shape also influences interactions. Anisotropic particles

Received: June 13, 2019
Published: June 17, 2019

DOI: 10.1021/acs.langmuir.9b01811
Langmuir 2019, 35, 9274–9285

interact in complex manners influenced by features such as facets and edges or highly curved sites.[6−10] In all of these settings, the alignment of the liquid crystal molecules on colloid surfaces and at the boundaries of the domain plays a central role in setting the energy landscape.

Nematic liquid crystals are rodlike molecules that coalign with their neighbors. The average molecular orientation at any location defines the director **n**, a headless vector. The molecular orientation at boundaries is defined by surface chemistry or texture to be either homeotropic (perpendicular) or planar (tangent to the bounding surface). Deviations of the director field from a uniform orientation via bend, twist, or splay incurs elastic energy penalties.[1] The behavior of colloids in an oriented director field depends on the colloid radius a. The surface energy of a colloid scales with Wa^2, and the bulk elastic distortion energy scales with Ka, where W is the surface energy density (= [J/m^2]) and K is the bulk energy density (= [J/m]). The ratio of the two quantities defines the extrapolation length $\xi = \frac{K}{W}$. Using typical elastic constants $K = 10^{-11}$ N and $W \approx 10^{-4} - 10^{-5}$ J m^{-2},[11] the extrapolation length is estimated to be $\xi \approx 0.1-1$ μm. Particles smaller than ξ introduce very little bulk distortion. Particles larger than ξ introduce a significant distortion; such colloids are typically accompanied by topologically required companion defects. For example, a homeotropic colloid in NLC introduces a topological charge of +1.[12] This charge can be compensated for by a companion hedgehog defect, a small melted region in the domain adjacent to the colloid with −1 topological charge. In this configuration, the colloid and companion defect form a dipolar pair (Figure 1a). Alternatively, the companion defect

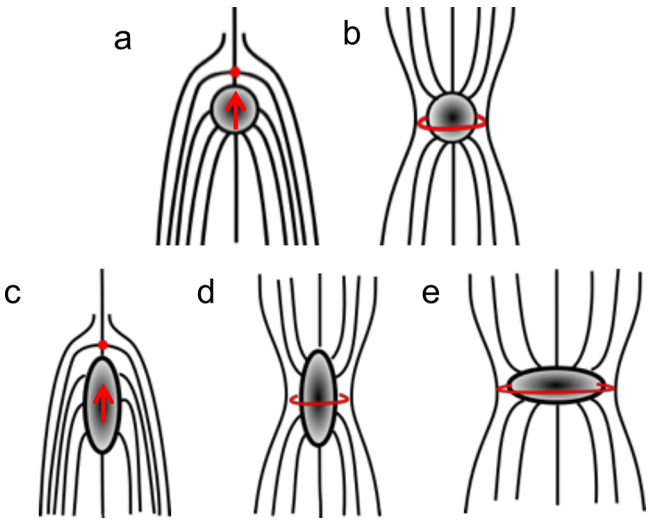

Figure 1. Spheres and ellipsoids of homeotropic (perpendicular) anchoring in an NLC. Schematics of (a) a dipole around a sphere, (b) a Saturn ring around a sphere, (c) a dipole around an ellipsoid, (d) Saturn I, and (e) Saturn II. Defects are highlighted in red, and the nematic director is represented by the dark solid lines.

can be in the form of a Saturn ring, a disclination line encircling the particle (Figure 1b). This configuration has quadrupolar symmetry. While the dipolar and quadrupolar forms are topologically equivalent, they differ significantly in their range of interactions. In the far field, by analogy to electrostatics, these colloids and companion defects interact and assemble in a manner similar to charge multipoles. The equilibrium structure depends on the size of the particle. For particles with diameters of hundreds of nanometers, the Saturn ring configuration is stable, whereas the dipolar configuration is favored for microscale particles. The Saturn ring can be stabilized by external fields[13] or by confinement.[14] We use this latter stabilization mechanism in our studies. Ellipsoidal colloids also impose defects and generate companion defects in an otherwise uniform director field.[15] Homeotropic ellipsoids in NLCs generate three distinct configurations. The hedgehog or dipolar defect configuration has the colloid's major axis aligned with the far field director (Figure 1c). The axisymmetric quadrupolar configuration has a small Saturn ring in the plane defined by the two minor axes, and the colloid's major axis is aligned with the far field director (Figure 1d). Finally, a second Saturn ring configuration has the major axis perpendicular to the far field director and a defect loop that wraps the ellipsoid lengthwise (Figure 1e). We refer to the latter two configurations as Saturn I and Saturn II, respectively.

Defects not only appear around particles but also can be forced to appear in the bulk and on surfaces.[12,16] By tailoring the boundary conditions, defects can be designed to template the assembly of particles.[17] For example, particles are attracted to disclination lines, assembling along them like pearls on a chain.[16,18] Disclination lines can be elongated and pulled to desired locations using laser tweezers[19] or manipulated in microfluidics devices.[20] The malleability of disclination lines makes them versatile sites for assembly. However, the strength of particle−disclination line interactions typically traps particles,[21] impeding the ability to reconfigure particle arrangement.

We became intrigued with the idea of making gentler cues that could guide particles to particular loci but could also allow reconfiguration. To avoid strongly trapped states associated with colloidal assembly within defects, we have developed a defect-free host NLC director field adjacent to a wavy wall. Our approach complements those based on patterned anchoring on bounding surfaces,[22,23] which can also impose gentle distortions in the nematic director field. The wavy wall, with alternating hills and wells, imposes a gentle distortion with well-defined regions of bend and splay. Regions of bend are easily understood as regions where the director field curves without twisting, characterized by nonzero $\mathbf{n} \times (\nabla \times \mathbf{n})$. Regions of splay correspond to domains with finite divergence in the director field $\nabla \cdot \mathbf{n}$. Sites of converging splay are like those above the well, where the director field lines converge to a point. Sites of diverging splay are like those above the hill, from which the director field lines diverge. The alternating hills and wells, formed by intersecting arcs of radius R, can be approximated as waves of wavelength λ and amplitude $\mathcal{A}$ (Figure 2a). The experimental platform consists of an epoxy strip, treated with surfactant dimethyloctadecyl[3-(trimethoxysilyl)propyl]ammonium chloride (DMOAP) to have homeotropic anchoring. This strip is sandwiched between two glass coverslips with planar anchoring (Figure 2b). We observe the sample under optical microscopy from a bird's-eye view, allowing us to observe the full dynamic trajectory. In the absence of particles, the domain is defect-free. When introduced into this domain in the vicinity of the wall, particles and their companion defects distort the surrounding director field and are attracted to boundary locations with complementary distortions. This is the basis of lock-and-key interactions[24] (Figure 2c,d).

DOI: 10.1021/acs.langmuir.9b01811
Langmuir 2019, 35, 9274−9285

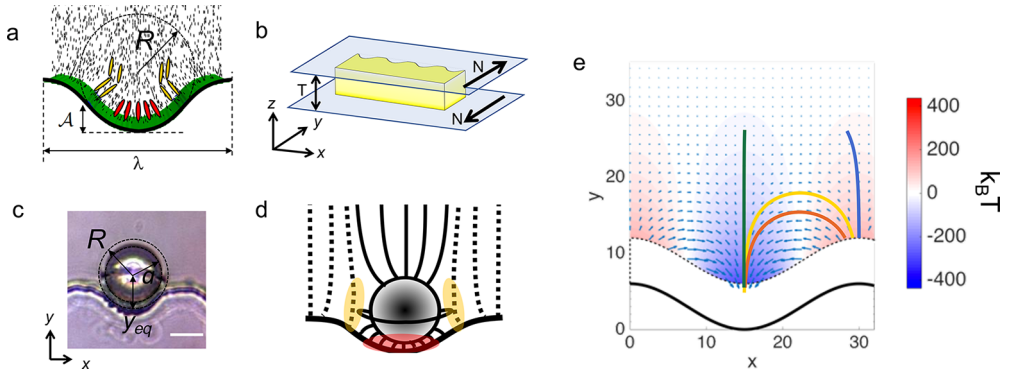

Figure 2. (a) Sketch of the system geometry. λ, R, and $\mathcal{A}$ are the wavelength, radius of curvature, and amplitude of the well, respectively. Red and yellow rods denote exaggerated director field regions of splay and bend, respectively. (b) Schematic of the experimental setup. (c) Lock-and-key docking of a particle near a wall. The scale bars is 10 μm. a is the size of the colloid, and y_{eq} is the equilibrium position of the center of mass (COM) of the colloid near the wall. (d) The "like likes like" colloid equilibrium configuration is characterized by matching splay (red highlighted region) and bend (yellow highlighted region) deformations. (e) Energy landscape and a few sample trajectories for a Saturn ring near a shallow well. (Reproduced from ref 27 by Luo et al. is licensed under CC BY (https://creativecommons.org/licenses/by/4.0/legalcode)).

In prior work, we explored the behavior of spherical particles as a function of wall geometry. Colloids adjacent to wavy walls differ strongly from colloids near flat walls. For example, spheres with homeotropic anchoring in sandwich cells are repelled from flat walls with oriented planar anchoring.[25] Near the wavy wall, however, a colloid in a Saturn ring configuration migrates to wells to find an equilibrium position. Depending on the well shape, the spherical colloid can be located either immediately next to the wall near the contact[26] or at distances comparable to several particle radii.[27] In approaching the wall, the colloid eliminates a volume of highly distorted liquid crystal. The equilibrium site, however, is influenced by details of the director field. In one mode of wall−colloid interaction, we observed "splay-matching" (i.e., the center of mass of a colloid with an undistorted Saturn ring equilibrates at a distance y_{eq} equal to the radius of curvature R of the well (Figure 2c)). At this location, the splay emanating from the surface of the colloid matches that from the wall, minimizing the distortion in the domain (Figure 2d). For deep or wide wells, this simple geometric rule must be modified. As the colloid approaches the wall, the Saturn ring shifts away from the wall. At equilibrium, the colloid sits deeper in the well, and the configuration has slightly dipolar character with significant bend adjacent to the colloid that coincides with bend at the edges of the well. In both cases, the colloid and wall attraction can be understood in terms of complementary distortion fields, that is, regions of bend (shown in yellow) or splay (shown in red) adjacent to the colloid matching those near the wall (Figure 2d). These concepts can be extended to understand wall−colloid repulsion and to tune the trajectories of colloids in NLCs. Hills are repulsive, as evidenced by the fact that the director field above a hill is highly incompatible with the distortion from the colloid. Using a Landau−de Gennes approach, the nematic director field and associated elastic energy field around the colloid can be found as a function of colloid location. This energy landscape is shown as the heat map in Figure 2e. By taking gradients of this energy landscape, forces on the colloid as a function of colloid location can be found. The force field is shown as the vector field in Figure 2e. Depending upon its initial location, a particle can follow a range of trajectories. In particular, a quadrupolar colloid above a hill is in an unstable position. The colloid can be repelled along multiple diverging paths depending upon its initial position. Thus, colloids can be propelled away from boundaries or drawn to adjacent wells, and these different fates are very sensitive to the particle's initial location. These forces originate in the nematic director field, controlled here by anchoring conditions of the vessel boundary and colloid. Notably, these forces do not depend on the particular material of the particles or boundaries, so particle motion and docking can be exploited to build structures from diverse materials. In our study of wall−spherical particle interactions, the wavelength of the features determines the range of the wall-sourced distortion, and the particle radius relative to the wall radius of curvature plays a strong role in determining the particle docking location.

It is a natural extension to probe the behavior of prolate ellipsoidal particles in this setting because the surfaces of these particles have smoothly varying curvatures to introduce a complex distortion field. In this research, we explore the behavior of an ellipsoid near a shallow well of curvature and width similar to the colloid diameter and note the equilibrium position realized by the colloid in relation to various geometry parameters. Thereafter, we study ellipsoidal particle interactions with deep narrow wells. Finally, we study ellipsoids with different aspect ratios near "through-pore" geometry.

EXPERIMENTAL SECTION

Preparation and Surface Treatment of Ellipsoids. Ellipsoidal particles are fabricated by a controlled stretching procedure from spherical polystyrene (PS) particles.[28] The PS particles ($2a$ = 10 μm and $2a$ = 25 μm) are embedded in a polymer matrix by dispersing two drops of stock solution in 20 mL of a 5 wt % poly(vinyl alcohol) (PVA) solution (average MW 85 000−124 000, 87−89% hydrolyzed) and swirled to mix. The solution is placed in a Petri dish to dry over the course of 2 weeks. The dried film is then cut into strips and clamped on both sides. The strip is stretched to twice its original length continuously while being heated with a heat gun (~500 °C) to stretch the PS particles along with the PVA matrix. The stretched films are then dissolved in a 80:20 DI water/isopropanol solution via sonication. Finally, the particles are washed three times with DI water (1960 rpm, 5 min). The ellipsoids are characterized by scanning electron microscopy (Figure S1a).

The surfaces of these particles must be functionalized in order to impose homeotropic anchoring. This requires that we first coat them with silica or metal. Chemical vapor deposition or sputtering leads to rough surfaces with associated contact line pinning. Therefore, solution processing is preferable. The following procedure has been adopted from ref 29. The stretched PS particles are dispersed in DI

DOI: 10.1021/acs.langmuir.9b01811
Langmuir 2019, 35, 9274−9285

water (~1 wt %), 8.28 mL of the solution is combined with 61.1 mL of ethanol and 10.1 mL of ammonia in a bottle, and the content is constantly stirred. A 5 wt % solution of TEOS (tetraethyl oscilicate) is slowly added at the rate of 1 mL every 25 mins. A total of 5 mL of solution is added. The particle is recovered and washed by centrifugation (1790 rpm, three times). The coating process results in surface imperfections with rough deposits on the order of 100 nm in height (Figure S1b,c), which may pin the Saturn ring disclination line. Once the particle is coated with silica, it is treated to give homeotropic anchoring by immersing particle in a 3 wt % DMOAP solution following by rinsing and heating for 1 h at 80 °C.

Assembling of the Cell. The cell fabrication procedure follows that in refs 26 and 27. Briefly, a strip with a wavy boundary that defines the hills and wells, deep wells, and pores is drawn using computer-aided design software (AutoCAD, Autodesk, Inc., San Rafael, CA, USA). The designs are transferred to a transparent photomask (CAD/ART Services Inc., Bandon, OR, USA). To fabricate the strips, we spin coat SU-8 2025 photoresist (MicroChem, Newton, MA, USA) on precleaned glass coverslips (Fisher Scientific, Hampton, NH, USA) and subsequently expose them to UV light through the mask to cross-link the exposed regions of the resist. Unexposed regions are etched away by immersing the coated glass inside a developer solution (Microchem, Newton, MA, USA). To obtain homeotropic anchoring on the features, they are first coated with silica by chemical vapor deposition. Silanization is carried out by immersing the silica-coated surface in a 3 wt % dimethyl octadecyl[3-(trimethoxysilyl)propyl] (DMOAP) solution for 10 min. The structure is rinsed with deionized water and cured on a hot plate at 80 °C for 1 h.

The two coverslips are coated with polyimide and rubbed with a velvet cloth to have uniform planar anchoring. The silica-coated functionalized SU-8 strip that defines the wall geometry is then carefully placed between the coverslips to form a planar cell "sandwiching" the strip. The two coverslips are assembled so that they have antiparallel-oriented planar anchoring. The coverslips are adhered with UV-sensitive glue to the strip to maintain the spacing between them.

We use nematic liquid crystal 5CB (4-cyano-4′-pentylbiphenyl, Kingston Chemicals) as purchased. The coated ellipsoids are dispersed inside the liquid crystal prior to each experiment because the PS tends to swell in liquid crystals. Generally, the liquid crystal is introduced into the cell by capillarity. Afterward, the cell is sealed with optical glue (Norland Products Inc., Cranbury, NJ). For pores, however, because the presence of small features tends to trap bubbles, liquid crystal is placed on the feature prior to sealing the cell.

Imaging. The cells are imaged using an upright microscope (Zeiss AxioImager M1m) in transmission mode equipped with crossed polarizers. All images shown in this article are in bright-field mode, but cross-polarized images are taken to verify the anchoring. The images are captured by a high-resolution camera (Zeiss AxioCam HRc). Objective magnification ranges from 20× to 50×. Image processing to track trajectories is carried out using open-source software FIJI.

Simulation. The details of the simulation method have been published previously[27,30] and are described in detail in ref 31. Key concepts are given briefly here. Landau−de Gennes simulations are a standard numerical method in solving for the director field without prior knowledge of the position of the defect. They are useful tools in elucidating our experimental findings. This approach uses a phenomenological model that uses a tensorial order parameter $\mathbf{Q}$ to describe the biaxial ordering of the molecules. In the uniaxial limit

$$\mathbf{Q}_{\alpha\beta} = \frac{3}{2}S\left(n_\alpha n_\beta - \frac{1}{3}\delta_{\alpha\beta}\right) \tag{1}$$

The geometry of the system, the boundary conditions, and elastic constants for the NLC are inputs to the numerical relaxation procedure. The total energy of the system

$$F = \int [f_{\mathrm{LdG}} + f_{\mathrm{boundary}}]\, \mathrm{d}V \tag{2}$$

is minimized with a finite difference scheme on a regular cubic mesh. F_{LdG} consists of two terms, f_{phase} and f_{d}, which can be expressed as the variation in the order parameter, S,

$$\begin{aligned} f_{\mathrm{phase}} &= \frac{1}{2}Atr\mathbf{Q}^2 + \frac{1}{3}Btr\mathbf{Q}^3 + \frac{1}{4}C[tr(\mathbf{Q}^2)]^2 \\ &= \frac{3}{4}AS^2 + \frac{1}{4}BS^3 + \frac{9}{16}CS^4 \end{aligned} \tag{3}$$

where A, B, and C are constants. In this expression, the term weighted by A drives the transition, the B term guarantees the asymmetry of S, and C bounds the values of S.[32] The constants used in the simulations are as follows, unless otherwise specified: $A = -0.172 \times 10^6$ J m^{-3}, $B/A \approx 12.33$, and $C/A \approx -10.06$, commonly used to model 5CB.

$$f_d = \frac{L}{2}\frac{\partial Q_{ij}}{\partial x_k}\frac{\partial Q_{ij}}{\partial x_k} \approx \frac{9}{4}LS^2\frac{\partial n_\alpha}{\partial x_i}\frac{\partial n_\alpha}{\partial x_i} \tag{4}$$

The elastic constant is $L = 2/9K/S^2 = 8 \times 10^{-12}$ N.

Numerical cost prohibits simulation on the experimental scale, so simulations are commonly performed on smaller systems. We simulate particle sizes roughly 100 times smaller than in experiment and set the anchoring strength to be about 100 times larger than in the experiment to have similar ratios of particle size to extrapolation length as in experiment. Our simulated ellipsoids have semiaxes of ~50−100 nm. In addition to the extrapolation length, nematic liquid crystals have an additional physicochemical length scale, the correlation length, which characterizes the size of the defect core and sets the scale of the mesh size Δx used in the simulations. The correlation length in 5CB is on the order of several nanometers.

Simulation variables are scaled with respect to characteristic energy densities and length scales that appear in the Landau−de Gennes (LdG) free-energy functional whose dimensional magnitudes are selected to relate to experiment, following the discussion in ref 32. The characteristic energy density is A, the material constant weighting the first term in the phase free energy in the LdG functional. The anchoring strength W is then made dimensionless by scaling the product of $|A|$ and Δx.

We model anchoring strengths in dimensional form as $W \approx 1 \times 10^{-2}$ J m^{-2}, or, in nondimensional form, $W = 12.9$ for finite homeotropic anchoring. For planar anchoring, in dimensional form, $W_0 \approx 1.5 \times 10^{-5}$ Jm^{-2}, corresponding to a value of $W_0 = 0.0193$ in nondimensional form. As noted above, these values are stronger than those that apply in the experiment by roughly the same factor as the inverse of the length rescaling (~10^2) so that the ratio of colloid size to extrapolation length $\xi = L/W$ is similar at both size scales. Additional details are given in the Supporting Information (Supplemental Note 1). Defects are defined as the regions where the order parameter S is significantly less than the bulk value. We chose $S < 0.9S_0$, where S_0 is the bulk value. For model constants typical for 5CB, $S_0 \approx 0.533$. The equal-constant approximation is used. The energy in simulation units is converted to real units (1 s.u. = $3.7k_BT$). The wall shapes are written separately by MATLAB and imported into the code as a boundary condition. The convergence criterion is set to be a decrease in energy per step of less than 1×10^{-4}, which corresponds to $3.7 \times 10^{-4}k_BT$ in energy.

Ellipsoids are simulated as follows

$$\left(\frac{x^2}{\alpha^2}\right)^p + \left(\frac{y^2}{\alpha^2}\right)^p + \left(\frac{z^2}{\beta^2}\right)^p = 1 \tag{5}$$

where $p = 1$. α and β are again the major and minor axes of the ellipsoid. x, y, and z define the local coordinate of the ellipsoid. Ellipsoid rotation is realized by defining a tilt angle of the ellipsoid's long axis with respect to the global director field.

The energy landscape of colloids near a wall (Figure 5c,d and Figure S3) are computed by moving the COM of the colloids on a grid separated by 9 nm and plotting the resulting values on a color map. The force experienced by the particles is computed by taking the gradient by a center difference method of the energy values. When simulating dipoles in the form of the "tip-ring" configuration, the core

DOI: 10.1021/acs.langmuir.9b01811
Langmuir 2019, 35, 9274−9285

energy of the defect is increased 2.6× by modifying the ratios of B/A and C/A with $B/A = 106$ and $C/A = -86.5$. With $A < 0$ held fixed, this replacement increases the minimum absolute value of f_{phase} (eq 3) by a factor of 2.6, and the director field is initialized with a dipolelike configuration to capture the higher-energy state of this configuration,[33] as explained in detail in ref 27. When we simulate the system with increased core energy, $S_0 \approx 0.427$.

The simulations identify minima of the Landau−de Gennes free-energy functional and the resulting defect and director field configuration. Thus, elastic energy fields from the undulating walls or trends in the elastic energy fields revealed by moving colloids with dipolar or Saturn ring defect configurations around the domain are relevant in interpreting the experimental findings. It is important to note, however, that even after matching the extrapolation length to the particle size one still cannot faithfully reproduce all experimental phenomena in simulation. These systems cannot be simply recast in nondimensional form because of the correlation length, which does not scale with the particle length scale. Because of the correlation length, there are known and significant differences between simulation and experimental scales. For instance, while dipoles are the most commonly observed defect form for micrometer-sized particles, in simulation, only Saturn rings are observed for particles that are several hundred nanometers in diameter. In our study, we use simulation for qualitative guidance.

RESULTS AND DISCUSSION

To study ellipsoidal particles with homeotropic anchoring, we fabricate particles with controlled anchoring by coating silica on the surface of stretched polystyrene (PS) particles. To avoid deleterious effects associated with the swelling of PS in the NLCs and degradation of the anchoring, we perform all experiments within 3 days of introducing ellipsoids into liquid crystal. PS particles of two different sizes ($2a$ = 10 and 25 μm) are stretched. Details are given in the Experimental Section.

Ellipsoids Far from the Wall. We have performed control experiments to compare the behavior of homeotropic ellipsoids to prior observations of ellipsoids and other elongated particles.[6,15,34−36] Here, we discuss key findings that influence our understanding of colloid−wall interactions. We confine ellipsoids with semimajor axis α and semiminor axis β (Figure 3a) in sandwich cells filled with NLC. The top and bottom surfaces of these cells have oriented planar anchoring in an antiparallel arrangement to minimize the tilt from rubbing, separated by a distance h = 25−45 μm. Once confined in these cells, the orientation of the ellipsoid's major axis differs by some angle θ from the direction of the uniform far field director as defined by the rubbing direction **N**. We study particles with aspect ratio k from 1.5 to 7.5, where k is defined as $\frac{\alpha}{\beta}$. For smaller colloids (stretched from $2a$ = 10 μm PS particles) that are only weakly confined, we primarily observe dipolar structures with the hedgehog localized at the pole of the ellipsoid (Figure 3b,c), and only occasionally observe Saturn rings. While the dipole configuration was not discussed in ref 15., a dipolelike "tip-ring" configuration was simulated. In that study, the particles are much smaller (stretched from $2a$ = 2 μm PS particles). In ref 36, the dipole and Saturn ring coexist in a confined setting for rodlike particles (cross section $2a$ = 1.5 μm), but only Saturn II is observed. In our work, for larger particles (stretched from $2a$ = 25 μm PS particles) in cell thickness h = 25−35 μm, all three configurations are observed: dipole (Figure 3b,c), Saturn I (Figure 3d,e) and Saturn II (Figure 3f,g). They each occur 44, 23, and 32% of the time, respectively. When we place the same colloid (stretched from $2a$ = 25 μm PS particles) in cells of thickness h = 35−45 μm, only dipoles are observed.

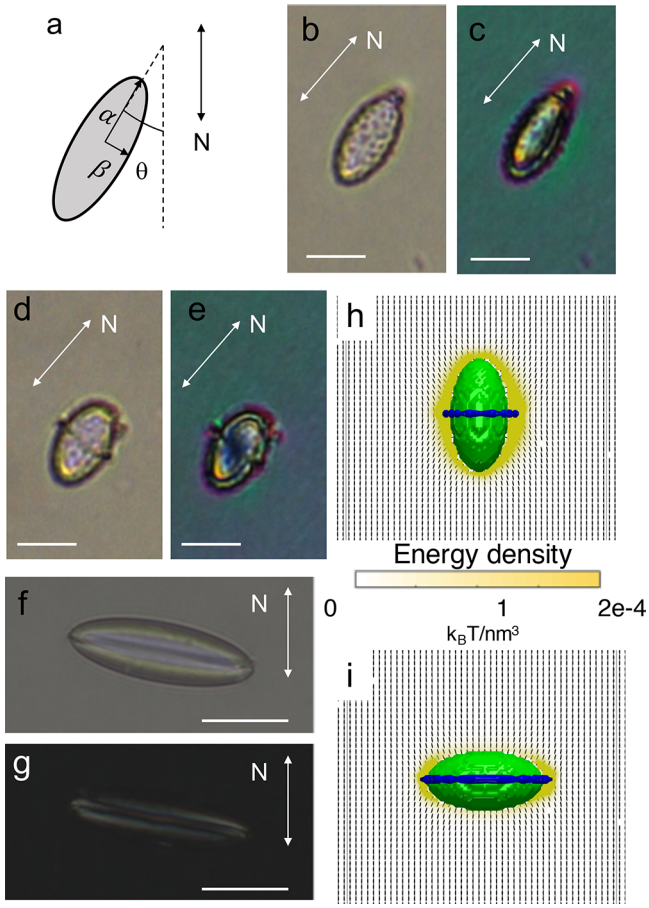

Figure 3. Defects and director field around ellipsoids far from the wall. (a) Schematic of an ellipsoid with semimajor axis α and semiminor axis β, oriented with its long axis at angle θ with respect to far-field director field N. (b, c) Bright field (BF) and cross-polarized (XP) images of a dipole. (d, e) Bright field (BF) and cross-polarized (XP) images of a Saturn I. (f, g) Bright field (BF) and cross-polarized (XP) images of a Saturn II. (h, i) Elastic energy density around (h) Saturn I and (i) Saturn II. Simulation colloids have semimajor axis α = 90 nm and semiminor axis β = 45 nm. Scale bars are 10 μm in b−e and 25 μm in f and g.

Ellipsoids with dipolar and Saturn I configurations orient along angles distributed around the rubbing direction **N** (i.e., around θ = 0° (Figure S2)), while Saturn II configurations align along angles distributed around θ = 90° (Figure S2). Simulation of the elastic energy in ref 15 reveals several behaviors relevant to our studies. First, the Saturn II configuration is the equilibrium state far from the wall under strong confinement ($h \leq 2\beta$). The dipole is the equilibrium configuration for microscale unconfined prolate ellipsoids as it is for spheres. Second, the Saturn I configuration is degenerate in θ for angles of less than 15° (i.e., there is no torque for small θ to enforce alignment until some critical angle). For k = 3, there is a plateau in the energy of the system; for k = 5 and 7, the plateau becomes a secondary minimum. The energy gradient near θ = 90° is also weak. These findings may explain the wide distribution of alignment angles observed in the experiment, although Saturn ring pinning at rough sites on the particle surface may also play a role. Third, the distribution and strength of distortions in the director field differ strongly for

DOI: 10.1021/acs.langmuir.9b01811
Langmuir 2019, 35, 9274−9285

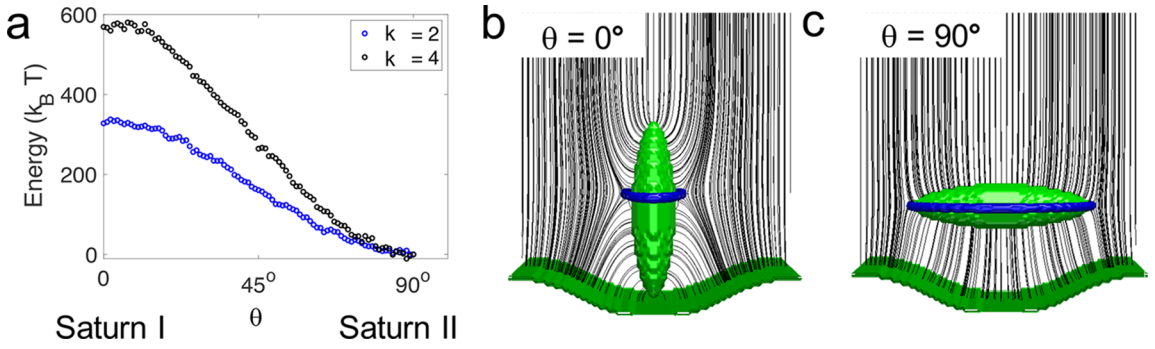

Figure 4. (a) Total energy of the system as the colloid goes through rotation from $\theta = 0$ to 90° configuration when the COM is located at $y = 153$ nm for $k = 4$ and at $y = 99$ nm for k = 2. (b, c) Simulation snapshots of $\theta = 0$ and 90° configurations for a $k = 4$ ellipsoid where $y = 153$ nm. In the simulation, colloids have a semimajor axis $\alpha = 143$ nm and a semiminor axis $\beta = 36$ nm.

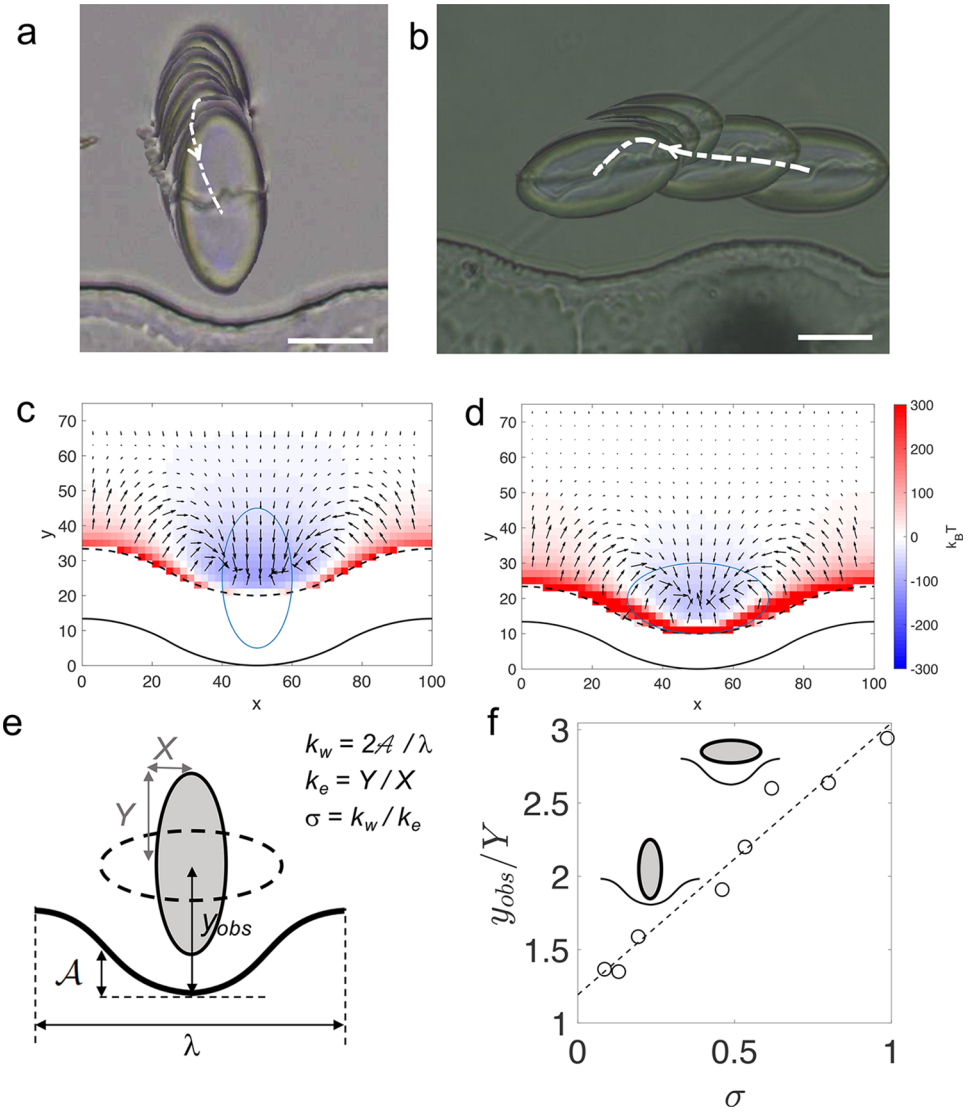

Figure 5. Ellipsoid docking near the shallow well. (a, b) Composite images of the full trajectories of ellipsoids of $k = 2$ for (a) Saturn I, also in Supporting Information video 1, and (b) Saturn II, also in Supporting Information video 2. White dotted lines denote trajectories of the COM. The scale bars are 25 μm. Energy landscape for (c) Saturn I and (d) Saturn II near shallow wells. Simulations of the total energy of the system are presented on the color map, and the gradient is computed to show the force field assuming no tilting during migration. Semimajor axis $\alpha = 90$ nm and semiminor axis $\beta = 45$ nm. Blue ellipses denote the position of the ellipsoid when the system is in its lowest-energy state. A solid line denotes the wall. The dashed line denotes the excluded region next to the wall. (e) Schematic of an ellipsoid right next to the wall, with wavelength λ and amplitude $\mathcal{A}$. $x = \beta$, $y = \alpha$ for $\theta = 0°$ and vice versa. (f) Open dots denote the normalized COM of the ellipsoids y_{obs}/Y versus σ, the ratio of aspect ratios. The dashed line serves as a guide to the eye.

DOI: 10.1021/acs.langmuir.9b01811
Langmuir 2019, 35, 9274−9285

the two Saturn configurations. Guided by the simulation of a colloid of the same k for Saturn I and II, we note that the Saturn II configuration has strong splay distortions isolated near the highly curved tips (Figure 3i), while the distortion density around Saturn I is generally more uniformly distributed around the colloid (Figure 3h).

These differences in the distortions around the Saturn configurations suggest that the forces on Saturn I and II should have different ranges and strengths of interaction. The Frank free energy, valid for weak distortions, can be used to arrive at scaling arguments. In the one constant limit, the Frank free energy reads[1]

$$F = \frac{K}{2}\int[(\nabla\cdot\mathbf{n})^2 + (\nabla\times\mathbf{n})^2]\,dV \tag{6}$$

where the integration is taken over a volume in which the nematic order is nonsingular. In the Saturn II configuration, the strong distortion near the tips can be approximated as $\sim K\beta$, whereas the distortion along the length of the Saturn I configuration can be approximated as $\sim K\alpha$. The LdG simulation, valid for large distortions, supports these scaling arguments in that the amount of distortion is roughly proportional to the semiaxis of the colloids (Figure 3h,i). Experiments indicate that the range of interaction between a pair of particles is approximately equal to the size of the particles.[34,36] A related argument has been used to justify the transition to the nonaggregated state of long k ellipsoids with planar anchoring.[35]

For the Saturn II configuration, the regions of strong distortion at the tips are highly sensitive to perturbations in the bulk director field and play a strong role in wall interactions.

Ellipsoid near Shallow Wells: Saturn Configurations. We study ellipsoids near shallow wells, for which the amplitude of the wall geometry $\mathcal{A}$ is much less than the wall radius of curvature R and the colloid length 2α is comparable to the well width $\lambda/2$, as defined in Figure 2a. Particles in both Saturn I and II configurations equilibrate at some distance from the bottom of the well, roughly centered above the well. Furthermore, both configurations persist, even near wells whose curvature is more compatible with the Saturn II configuration. Ellipsoids initially in Saturn I configurations enter wells with only small changes in angle along their paths and remain in a nearly upright position. Ellipsoids initially in Saturn II configurations find nearly horizontal positions. Simulation shows that the Saturn II configuration indeed has the global minimum energy. We suspect that the Saturn I configuration is stabilized by the degeneracy of the energy to the inclination angle for small tilt angles reported for colloids in the bulk. Indeed, simulation reveals that this degeneracy persists close to the wall. This is shown in Figure 4a, in which the total elastic energy of the system is shown for ellipsoids with their centers of mass fixed at some height (y = 153 nm) above the well as a function of angle θ for k = 2 and 4. Note that a plateau exists for k = 4 but only a weak gradient exists for k = 2. Thus, for Saturn I configurations with only weak inclination angles, there is no torque to drive rotation to the equilibrium Saturn II configuration. Images of the director field for colloids in their minimum-energy state for fixed horizontal (Saturn II) and vertical (Saturn I) orientations are shown in Figure 4b,c. The orientation of the colloid is an input to the simulation, just like the experiment, and here we consider the Saturn I configuration to be effectively metastable.

We track the position of the ellipsoids with Saturn I (Figure 5a) and Saturn II (Figure 5b) with k = 2 (Supporting Information videos 1 and 2). For spherical colloids in shallow wells with widths similar to the colloid radius, the Saturn ring remains at the equator of the colloid and the concept of splay matching captures the particle's equilibrium location. The splay fields emanating from the ellipsoids near the walls generated by the tip for Saturn I and the side for Saturn II can also be estimated. However, at equilibrium, the Saturn I configuration finds a site far deeper in the well than would be expected from splay matching owing to the strong attraction between bend along the particle's sides and that at the well's edge. The Saturn II configuration equilibrates further from the wall than would be expected for splay matching because of strong repulsion between the Saturn ring and the wall for this configuration. To gain deeper insight, we simulate the total elastic energy in the system for a colloid at various locations near the well, as reported in Figure 5c,d for the two Saturn configurations for a colloid with α = 90 nm and β = 45 nm.

For fixed colloid orientation, the center of mass of the particle is placed at points separated by 9 nm on a square grid that discretizes the domain within one wavelength from the wall. In these figures, the thin black line indicates the wall location, and the dashed blue line adjacent to the wall is an excluded region where the particle would overlap the wall geometry. The reference energy is the total energy of the system when the particle is situated one wavelength above the well at the centerline. The colloid (blue ellipsoid) is shown at its equilibrium position. By moving toward the wall, the ellipsoid replaces regions of strong deformation and enables particle-sourced splay and bend deformations that are compatible with those near the well. The elastic force field experienced by the ellipsoid is computed by using Newton's difference method to take the negative gradient in the elastic energy. The resulting vector field is graphed atop the energy landscape diagrams (Figure 5c, d). The force field for k = 4 is also computed and reported in the SI (Figure S3). These vectors define complex paths for ellipsoids with a fixed angle throughout their migration. We will explore the predicted paths in future work because the current particles are not ferromagnetic and cannot be easily reoriented or positioned by external magnetic fields. The simulated elastic force fields in Figure 5c,d includes the contributions from the complex director for the colloid confined in our system. To guide intuition, we discuss sites of compatible bend and splay with the wall. However, we study ellipsoids, objects of revolution, between top and bottom plates interacting with the undulating wall. The resulting director field is complex and three-dimensional. Distortions above and below the objects (i.e., between the colloid and the top and bottom planes) repel the colloid from those bounding surfaces.[25] Near-field details owing to the three-dimensional nature of the director field between the colloid and undulating walls likely also contribute to near-field repulsion and prevent the colloid from touching the undulated wall.

Thus far, we have shown that prolate ellipsoids interact via bend and splay near the wall with shallow undulations. The strength of this interaction can be characterized as a binding energy or difference in total system energy for a colloid far from the wall and at its equilibrium position. We chose the reference energy for this calculation when a colloid is located at y = 338 nm away from the wall and round the simulation results to 0.1 simulation unit. For ellipsoids of k = 2, the

DOI: 10.1021/acs.langmuir.9b01811
Langmuir 2019, 35, 9274−9285

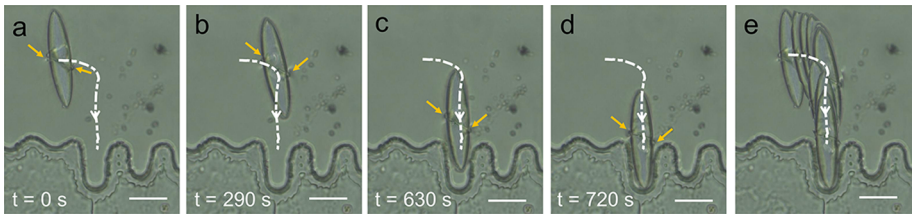

Figure 6. (a–d) Time-lapse images of an ellipsoid entering a deep well. The white dotted line denotes the trajectory of the COM of the migrating ellipsoid. (e) Composite image of the full trajectories of the ellipsoid. A video file of the migration can be found in Supporting Information video 3. The yellow arrows denote the location of the defect. The scale bars are 25 μm.

binding energy for the Saturn I configuration is (-144 ± 0.4) k_BT, while that for Saturn II is $(-81 \pm 0.4)k_BT$. Thus, the Saturn I configuration is more strongly bound, even though it always has a higher system energy. This might be ascribed to the strong distortion near the tips in the Saturn II configuration; near these poles, Saturn II experiences a repulsive region very near the wall, shown in red in Figure S4b.

We also find the total energy of the system when the colloid is located far from and close to the wall for ellipsoids with $k = 4$ (Figure S3) for the same wall geometry and ellipsoid volume. We conserve volume to mimic our system in which particles with different aspect ratios are obtained by stretching beads of fixed volume. As the colloid length becomes comparable to the well width, near-wall repulsion becomes more significant for Saturn II (Figure S3b). For these colloids, the binding energy for Saturn I is $(-129 \pm 0.4)k_BT$, while that for Saturn II weakens to a value of $(-52 \pm 0.4)k_BT$. Given that the bulk energy is $\sim Ka$, we may rescale the simulated elastic energy to find a rough estimate of the energies in the experimental system. These estimated binding energies are determined to be $(-3.2 \times 10^5)k_BT$, $(-1.8 \times 10^5)k_BT$, $(-2.9 \times 10^5)k_BT$, $(-1.2 \times 10^5)k_BT$ for Saturn I ($k = 2$), Saturn II ($k = 2$), Saturn I ($k = 4$), and Saturn II ($k = 4$), respectively. All trapping energies are much greater than thermal fluctuations, consistent with the deterministic paths followed by the objects. They are similar in magnitude to estimates obtained in prior research by analyzing spherical particles in the experiment in which viscous dissipation was inferred along a particle path.[26]

The distribution and type of distortion in the nematic director field depend on the particle shape. For a sphere, the distortion around it has splay and bend elements, with pronounced distortion near the defect ring. For ellipsoids in the Saturn I configuration, there is a strong bend along the sides and a strong splay at the poles, while the Saturn II configuration has strong bend and splay deformations at its equator, with only weak distortions on the top and bottom. Distortion fields decay nonuniformly around the ellipsoids in Saturn I and II configurations, yielding directionally dependent ranges of interaction which differ from a sphere of equal volume ($a^3 = \alpha \times \beta^2$). As expected from the scaling argument given above, the range of interaction in the direction along the far field director is greatest for Saturn I, followed by the sphere, followed by the Saturn II configuration. Perpendicular to this direction, the range is greatest for Saturn II, followed by Saturn I, followed by the equivalent volume sphere. For this reason, the Saturn I configuration interacts more strongly with the wells. These findings are corroborated by simulations that look at the decay of the distortion away from the colloids along the vertical and horizontal axes (Figure S4).

The observed particle trajectories show that the range of particle–wall interactions is indeed configuration-dependent. Saturn I configurations interact over distances comparable to the major axis length α, while Saturn II configurations interact over distances comparable to the minor axis length β. Typically, Saturn configurations do not migrate over distances longer than their geometric length scales. We have observed four instances where ellipsoids in Saturn II configurations migrate horizontally and hover above the well without actually docking (Figure S5). This may be partially attributed to the weak distortion gradient along the Saturn II sides (Figure 5d and Figure S4b).

To summarize these observations, we record the final position of ellipsoids above the well center line for colloids of varying k for well widths greater than the ellipsoid semimajor axis ($\lambda > 2a$). We define y_{obs} as the height of the colloids' center of mass from the base of the well center (Figure 5e). To relate the final position of the colloid to various geometric parameters of the system, we define the well aspect ratio $k_w = \frac{2A}{\lambda}$ and ellipsoid aspect ratio $k_e = \frac{Y}{X}$. In this quantity, X and Y are the lengths of the semiaxes in the x and y directions, respectively (Figure 5e). For the Saturn I configuration, $X = \alpha$, $Y = \beta$, and $k_e = k$, whereas for the Saturn II configuration, $X = \beta$, $Y = \alpha$, and $k_e = 1/k$. To capture the effect of well geometry, we define $\sigma = \frac{k_w}{k_e}$; for shallow wells, $\sigma < 1$. We plot the y location of the particle normalized by its semiaxis length along the y direction $\frac{y}{Y}$ against the quantity $\sigma = \frac{k_w}{k_e}$ (Figure 5f). We find σ to be the relevant parameter that captures the system's behavior. This scaling shows that the colloid equilibrium distance from the base of the well decreases with increasing colloid aspect ratio in its aligned direction k_e and that colloids above wider wells are located lower than colloids over narrower wells.

Particles Entering Deep Wells. While both Saturn configurations were able to interact with shallow wells, we expect narrow, deep wells to be accessible only to the Saturn I configuration owing to steric constraints. Furthermore, the Saturn II configuration should be repelled by the hills that we have placed adjacent to the deep wells and should fail to dock to the wall. Thus, interactions with the wall should be selective on the basis of colloid orientation. We expect Saturn I to dock, while Saturn II will not. To explore this behavior, we construct deep, narrow wells with nearly straight side walls and a circular arc at the base. The wall that we studied is shown in Figure 6. It features wall undulations with hills and wells of differing depths, all with widths comparable to the particle minor axis. The depth of the well equals α, and the bottom of the well is a semicircle of radius $R_{well} = 15$ μm. Indeed, we observe strong interactions between deep wells and Saturn I configurations. We have observed Saturn II configurations drifting above these high-frequency undulations without apparent attraction.

DOI: 10.1021/acs.langmuir.9b01811
Langmuir 2019, 35, 9274–9285

Figure 6a–d shows snapshots of an ellipsoid in the Saturn I configuration as it enters a well (Supporting Information video 3). The entire trajectory is shown as the white dashed line. The colloid is attracted over distances comparable to its major axis. Initially, the Saturn ring is pinned at a slightly tilted configuration as the particle moves into the well, and the tilting is gradually corrected, although not completely (Figure 6b,c). As the ellipsoid docks deep within the well, the ring shifts upward (Figure 6d). Figure 6e shows the change in particle position at equally spaced time increments, allowing changes in the rate of motion to be captured. As the colloid enters the well, it moves more rapidly in spite of its proximity to the wall and large associated hydrodynamic interactions, indicating steep energy gradients there; we associate this with the highly compatible bend and splay fields from the colloid and the wall. Recall that the microscope stage is horizontal; the insertion of a high aspect ratio object into this deep well is guided entirely by the nematic director field. Issues of well selection and range will be explored in future work.

As the ellipsoids interact with the wells, the Saturn rings can be displaced by interaction with the wall. Previously, we studied this displacement for spheres and found that elastic interactions with the wall can drive an irreversible quadrupole-to-dipole transition. We identified a critical angle of 130°, below which the ring could distort and recover and above which the transition was irreversible.[27] In this study, such a transition has not been observed for ellipsoids. However, a systematic study of disclination line displacement on ellipsoids is an interesting subject for future work given the complexity of the colloid shape, Saturn I and II configurations, and the well geometries.

Particle Plugging in Pores. Ellipsoids with dipolar defects also interact with the wavy wall structure; these interactions are similar to the interactions of spherical colloids with dipolar defects in that a dipole with its companion defect above it docks in a well (Figure 7a) while a dipole with its companion defect below docks on a hill (Figure 7b). Simulation reveals the director field of a dipole near a wall where dipoles are modeled by the tip-ring configuration (Figure 7c,d).

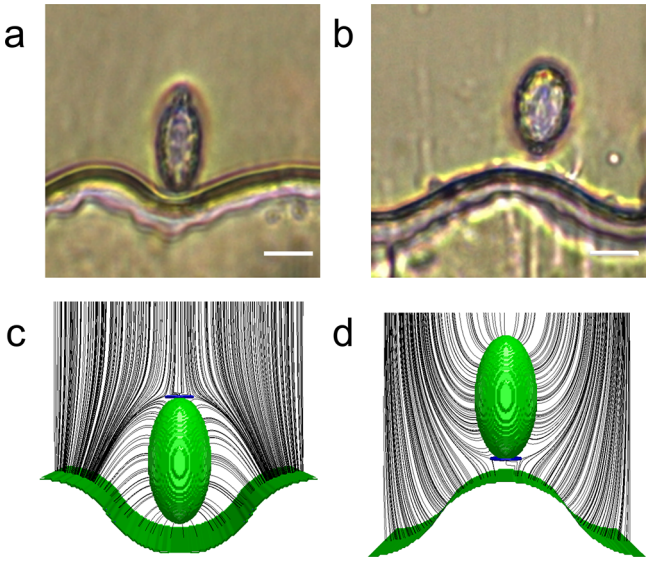

Figure 7. Docking behaviors of dipoles (aspect ratio k = 2). (a, b) Docking of dipoles when the dipole is oriented upward in (a) and downward in (b). The scale bars are 10 μm. (c) Simulations of the scenarios in (c) and (d) where the dipole is modeled as a small ring. Simulated colloids have semimajor axis α = 90 nm and semiminor axis β = 45 nm.

We also observed the interactions of dipoles and colloids in Saturn I configurations with highly displaced Saturn rings, which are not quite tip-ring configurations above the deep, narrow wells. When the defect points up, it docks just like ellipsoids with Saturn rings. However, as expected, ellipsoidal dipoles with companion hedgehog defects away from the wall are repelled and do not dock (Figure S6). For the highly displaced ring away from the wall, docking occurs in a manner similar to that of Saturn I in Figure 6.

Having established that a nearly upright ellipsoid can insert within a deep and narrow well, we become intrigued with the idea that the colloids might be guided by regions of compatible distortion to enter and block pores connecting two domains. We explore a new type of well shape, a pore or "through-hole". In 2D, these through-holes are made up of protrusions from the wall resembling mushrooms in shape (Figure 8a). The interstitial sites between adjacent mushroom caps provide bend deformation and a passage toward a wide rectangular region at the back. The stem of the mushroom must be connected to a base in order to be removed as a strip and treated to have homeotropic anchoring. The director field in this geometry is visualized by simulation as shown in Figure 8b. One domain is highly confined with zones of strong bend–splay, like the pore, and the other less so, with a gently decaying bend–splay field.

We find that, for cell thicknesses that stabilize the Saturn ring around the ellipsoids, we also trap a defect ring around the mushroom cap. While the ring is not strictly required by topology, its formation is not surprising. We fabricate the cell in a way that leaves a small gap between the top of the feature and the glass coverslips that enforce planar alignment. In thicker cells, the director field has room to escape and does not form a defect. However, in thinner cells, this defect line appears regularly (Figure S7a). As colloids enter the through hole in the Saturn I configuration, the interaction between the Saturn ring and the defect near the mushroom cap is unavoidable. These interactions trap the colloid near the pore in tilted configurations with the tip of the colloid trapped by the defect (Figure S7b,c) before they interact with the opening.

To study colloid–pore interactions without such trapping effects, we focus on the behavior of dipoles, which form readily in cells of greater thickness. In these thicker cells, there are no disclination lines at the pore entrance. Ellipsoids in the pores find final positions in which they do not touch the neck of the mushroom, indicating that they are in equilibrium characterized by a balance of elastic forces. As a reference, we study spheres as well as ellipsoids with differing aspect ratios. Three typical particle–pore interactions are shown in the Figure 8c–e with increasing aspect ratio k. In particular, these ellipsoids appear in the order of increasing 2α (= 12, 40, 55 μm) but have approximately the same 2β (= 12, 17, 13 μm). The spherical colloids that are used have diameter $2a$ = 12 μm. Even though the ellipsoids were stretched from particles of roughly the same size, the slight polydispersity in the batch resulted in colloids with roughly the same β, and the presence of the well excludes ellipsoids of larger β from entering. Spherical colloids (k = 1, Figure 8c, Supporting Information video 4) and low-k ellipsoids (k = 2, Figure 8d, Supporting Information video 5) stop above the neck of the pore while for

DOI: 10.1021/acs.langmuir.9b01811
Langmuir 2019, 35, 9274–9285

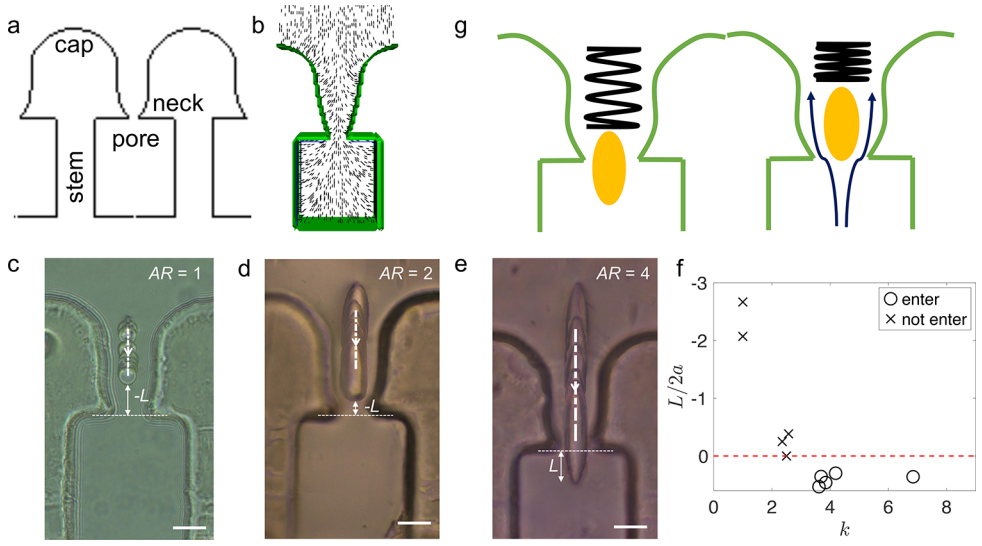

Figure 8. (a) Schematic of the through-hole wells. The gradient blue region denotes regions filled with NLC. (b) Simulated director field near the through-hole geometry. (c–e) Time-lapse images of (c) a sphere (k = 1) and Supporting Information video 4, (d) an ellipsoid (k = 2) and Supporting Information video 5, ad (e) an ellipsoid (k = 4) entering a through-hole and Supporting Information video 6. The white dotted lines denote the trajectory of the COM of the migrating ellipsoid. The scale is 25 μm. (f) k versus normalized entrance length $\frac{L}{2a}$. The dashed red line denotes a reference point, where the bottom of the particle aligns with the neck of the pore. (g) Schematic for one-way ball check valves that allow only material transport in one direction.

k = 4 (Figure 8e, Supporting Information video 6) the particle enters. To quantify the dependence of the equilibrium position on k, we measure the length of ellipsoids that goes beyond the neck of the pore as L (Figure 8e). If L < 0, then the ellipsoid sits above the pore and does not go through. There is a clear divide at k = 3, below which the ellipsoid does not enter the through-hole and levitates above the neck (L < 0). We find that L < 0 for small k and L > 0 for large k (Figure 8f). The entrance length L does not strongly correlate with the minor axis β (Figure S8 and Supporting Informatio note 2).

Colloids located in deep wells remove a highly distorted region of the nematic director field and have particle-sourced distortions that are compatible with those in the pore. These effects are also present for the part of the colloid that remains in the pore. However, as part of the colloid leaves the pore, it enters a region of gentle bend and splay that is far less confined. In this region, particle-sourced distortions can decay over longer length scales. The balance of these two effects determines the equilibrium location of colloids that span the pore. Colloids of smaller k never enter deeply enough into the pore to explore this region. Colloids of large-enough k enter, and the migration is irreversible. This structure is similar to a one-way ball check valve, as illustrated in Figure 8g. A ball valve is driven by a spring that pushes the ball along a tapered direction to form a seal. In our case, the ball (the ellipsoid) is driven to block the pore by the elastic force supplied by the LC. These through pores are a type of 2D membrane. Ellipsoids of the right dimension and aspect ratio can plug the pores, preventing the transport of a certain material across the membrane. Upon melting, the ellipsoid can be displaced from its plugged position and allow material exchange across the membrane.

CONCLUSION

We have studied ellipsoidal colloids in defect-free, gently distorted nematic director fields formed near undulating boundaries. Like confined prolate ellipsoids in oriented nematics far from undulating walls, the ellipsoids adopt three configurations. These include dipoles with major axes aligned with the far -field director with companion defects at their poles, Saturn I configurations with the major axis similarly aligned, and Saturn II configurations with the major axis perpendicular to the far-field director. The Saturn II configuration has lower energy than the Saturn I configuration, and the dipolar state has the minimum energy on the microscale. Furthermore, like their spherical counterparts, Saturn configurations are stabilized by confinement in the sandwich cell. For the two Saturn configurations far from the undulating walls, the elastic energy field is degenerate with respect to tilt angle for small tilt angles.[15] This behavior is preserved near walls. This allows the Saturn configurations to explore a small range of tilt angles and inhibits Saturn I configurations from rotating to the lower-energy Saturn II configuration anywhere in the domain. Thus, colloids in both configurations coexist and preserve their orientations as they interact with wavy walls. Interacting with small-amplitude undulations and shallow wells, dipoles dock on hills if their companion defects are toward the wall and in wells if they are away from it, and both Saturn configurations dock in wells. This is similar to spherical colloids. However, the range of interactions of the ellipsoids depends on the alignment and defect type. Colloids aligned with their major axis along the director field in dipolar and Saturn I configurations have large distortion energies along their length and interact over distances similar to their major axis. Saturn II configurations have weaker distortion landscapes and therefore interact more weakly and over ranges like their minor axes. Interaction strengths or binding energies for colloids at walls also differ. The strong bend along the sides of the Saturn I configuration strengthens well–particle binding, while repulsion between the wall and the strong distortion near the disclination ring in the Saturn II configuration has a weakening effects. We calculate force fields on the colloids with fixed orientation using the

DOI: 10.1021/acs.langmuir.9b01811
Langmuir 2019, 35, 9274–9285

Landau−de Gennes formulation and will probe particle paths in future work.

In this study, we study the particle−wall interaction above deep wells with depths smaller than colloid length. These walls interact selectively with colloids aligned with the far-field director. Colloids in the Saturn I configurations and dipolar configurations sense these wells over distances comparable to their major axis and insert themselves into deep wells at rates that indicate steep attraction in spite of strong hydrodynamic drag near the wall. We then develop the through-pore geometry with pores that connect two distinct domains of nematic liquid crystals. One domain is highly confined and shaped like a deep well with bend and splay to attract the colloid, and the other is wide and relatively unconfined. In this setting, we explore the ability of elongated objects to interact with bend−splay at the pore openings and block the pores. Sufficiently elongated colloids in dipolar configurations indeed enter the pore and find equilibrium locations blocking the pore entrance, guided by the elastic energy landscape. These pores form a type of membrane with one-way valves.

In conclusion, it is our hope that this work might inspire new investigations into colloidal systems that exploit the elastic energy landscapes in confined liquid crystals. The deliberate development and exploitation of fully three-dimensional director fields (e.g., with cholesteric liquid crystals) is the focus of a separate study by our group.[37] When combined with external fields, stimuli to reconfigure liquid crystals, or reconfigurable boundaries, the interactions explored here provide a basis for reconfigurable structures.

■ ASSOCIATED CONTENT

Supporting Information

The Supporting Information is available free of charge on the ACS Publications website at DOI: 10.1021/acs.langmuir.9b01811.

Videos 1−6 (ZIP)

Supplemental notes and figures and descriptions of the supplemental videos (PDF)

■ AUTHOR INFORMATION

Corresponding Author

*E-mail: kstebe@seas.upenn.edu.

ORCID

Yimin Luo: 0000-0002-9627-8722

Kathleen J. Stebe: 0000-0003-0510-0513

Author Contributions

[⊥]K.S. was a 2018 Langmuir lecturer and presented the content of this article.

Notes

The authors declare no competing financial interest.

■ ACKNOWLEDGMENTS

This material is based upon work supported by, or in part by, the U.S. Army Research Laboratory and the U.S. Army Research Office under grant W911NF1610288. The authors thank Giuseppe Boniello for useful discussions.

■ REFERENCES

(1) Gennes, P.-G. D.; Prost, J. *The Physics of Liquid Crystals*; Oxford University Press, 1993.

(2) Poulin, P.; Stark, H.; Lubensky, T.; Weitz, D. Novel colloidal interactions in anisotropic fluids. *Science* **1997**, *275*, 1770−1773.

(3) Vitelli, V.; Turner, A. M. Anomalous coupling between topological defects and curvature. *Phys. Rev. Lett.* **2004**, *93*, 215301.

(4) Muševič, I.; Škarabot, M.; Tkalec, U.; Ravnik, M.; Žumer, S. Two-dimensional nematic colloidal crystals self-assembled by topological defects. *Science* **2006**, *313*, 954−958.

(5) Tkalec, U.; Muševič, I. Topology of nematic liquid crystal colloids confined to two dimensions. *Soft Matter* **2013**, *9*, 8140−8150.

(6) Beller, D. A.; Gharbi, M. A.; Liu, I. B. Shape-controlled orientation and assembly of colloids with sharp edges in nematic liquid crystals. *Soft Matter* **2015**, *11*, 1078−1086.

(7) Senyuk, B.; Liu, Q.; Nystrom, P. D.; Smalyukh, I. I. Repulsion−attraction switching of nematic colloids formed by liquid crystal dispersions of polygonal prisms. *Soft Matter* **2017**, *13*, 7398−7405.

(8) Ravnik, M.; Škarabot, M.; Žumer, S.; Tkalec, U.; Poberaj, I.; Babič, D.; Osterman, N.; Muševič, I. Entangled nematic colloidal dimers and wires. *Phys. Rev. Lett.* **2007**, *99*, 247801.

(9) Muševič, I. *Liquid Crystal Colloids*; Springer, 2017.

(10) Lapointe, C.; Hultgren, A.; Silevitch, D.; Felton, E.; Reich, D.; Leheny, R. Elastic torque and the levitation of metal wires by a nematic liquid crystal. *Science* **2004**, *303*, 652−655.

(11) Kočevar, K.; Muševič, I. Surface-induced nematic and smectic order at a liquid-crystal−silanated-glass interface observed by atomic force spectroscopy and Brewster angle ellipsometry. *Phys. Rev. E: Stat. Phys., Plasmas, Fluids, Relat. Interdiscip. Top.* **2002**, *65*, 021703.

(12) Kleman, M.; Lavrentovich, O. D. Topological point defects in nematic liquid crystals. *Philos. Mag.* **2006**, *86*, 4117−4137.

(13) Stark, H. Saturn-ring defects around microspheres suspended in nematic liquid crystals: an analogy between confined geometries and magnetic fields. *Phys. Rev. E: Stat. Phys., Plasmas, Fluids, Relat. Interdiscip. Top.* **2002**, *66*, 032701.

(14) Gu, Y.; Abbott, N. L. Observation of Saturn-ring defects around solid microspheres in nematic liquid crystals. *Phys. Rev. Lett.* **2000**, *85*, 4719.

(15) Tasinkevych, M.; Mondiot, F.; Mondain-Monval, O.; Loudet, J.-C. Dispersions of ellipsoidal particles in a nematic liquid crystal. *Soft Matter* **2014**, *10*, 2047−2058.

(16) Harada, S.; Mitsui, T.; Sato, K. Micro-wires self-assembled and 3D-connected with the help of a nematic liquid crystal. *Eur. Phys. J. E* **2012**, *35*, 1−12.

(17) Wang, X.; Miller, D. S.; Bukusoglu, E.; De Pablo, J. J.; Abbott, N. L. Topological defects in liquid crystals as templates for molecular self-assembly. *Nat. Mater.* **2016**, *15*, 106.

(18) Lee, E.; Xia, Y.; Ferrier, R. C.; Kim, H.-N.; Gharbi, M. A.; Stebe, K. J.; Kamien, R. D.; Composto, R. J.; Yang, S. Fine golden rings: tunable surface plasmon resonance from assembled nanorods in topological defects of liquid crystals. *Adv. Mater.* **2016**, *28*, 2731−2736.

(19) Osterman, N.; Kotar, J.; Terentjev, E. M.; Cicuta, P. Relaxation kinetics of stretched disclination lines in a nematic liquid crystal. *Phys. Rev. E* **2010**, *81*, 061701.

(20) Sengupta, A.; Bahr, C.; Herminghaus, S. Topological microfluidics for flexible micro-cargo concepts. *Soft Matter* **2013**, *9*, 7251−7260.

(21) Lubensky, T. C.; Pettey, D.; Currier, N.; Stark, H. Topological defects and interactions in nematic emulsions. *Phys. Rev. E: Stat. Phys., Plasmas, Fluids, Relat. Interdiscip. Top.* **1998**, *57*, 610.

(22) Peng, C.; Turiv, T.; Zhang, R.; Guo, Y.; Shiyanovskii, S. V.; Wei, Q.-H.; de Pablo, J.; Lavrentovich, O. D. Controlling placement of nonspherical (boomerang) colloids in nematic cells with photo-patterned director. *J. Phys.: Condens. Matter* **2017**, *29*, 014005.

(23) Peng, C.; Turiv, T.; Guo, Y.; Shiyanovskii, S. V.; Wei, Q.-H.; Lavrentovich, O. D. Control of colloidal placement by modulated molecular orientation in nematic cells. *Sci. Adv.* **2016**, *2*, No. e1600932.

(24) Silvestre, N. M.; Patrício, P.; Telo da Gama, M. M. Key-lock mechanism in nematic colloidal dispersions. *Phys. Rev. E* **2004**, *69*, 061402.

DOI: 10.1021/acs.langmuir.9b01811
Langmuir 2019, 35, 9274−9285

(25) Pishnyak, O. P.; Tang, S.; Kelly, J.; Shiyanovskii, S. V.; Lavrentovich, O. D. Levitation, lift, and bidirectional motion of colloidal particles in an electrically driven nematic liquid crystal. *Phys. Rev. Lett.* **2007**, *99*, 127802.
(26) Luo, Y.; Serra, F.; Stebe, K. J. Experimental realization of the "lock-and-key" mechanism in liquid crystals. *Soft Matter* **2016**, *12*, 6027−6032.
(27) Luo, Y.; Beller, D. A.; Boniello, G.; Serra, F.; Stebe, K. J. Tunable colloid trajectories in nematic liquid crystals near wavy walls. *Nat. Commun.* **2018**, *9*, 3841.
(28) Ho, C.; Keller, A.; Odell, J.; Ottewill, R. Preparation of monodisperse ellipsoidal polystyrene particles. *Colloid Polym. Sci.* **1993**, *271*, 469−479.
(29) Hsu, C.-P.; Ramakrishna, S. N.; Zanini, M.; Spencer, N. D.; Isa, L. Roughness-dependent tribology effects on discontinuous shear thickening. *Proc. Natl. Acad. Sci. U.S.A.* **2018**, 5117.
(30) Luo, Y.; Serra, F.; Beller, D. A.; Gharbi, M. A.; Li, N.; Yang, S.; Kamien, R. D.; Stebe, K. J. Around the corner: Colloidal assembly and wiring in groovy nematic cells. *Phys. Rev. E: Stat. Phys., Plasmas, Fluids, Relat. Interdiscip. Top.* **2016**, *93*, 032705.
(31) Beller, D. A. *Controlling Defects in Nematic and Smectic Liquid Crystals Through Boundary Geometry*. Ph.D. thesis, University of Pennsylvania, 2014.
(32) Ravnik, M.; Žumer, S. Landau−de Gennes modelling of nematic liquid crystal colloids. *Liq. Cryst.* **2009**, *36*, 1201−1214.
(33) Stark, H. Physics of colloidal dispersions in nematic liquid crystals. *Phys. Rep.* **2001**, *351*, 387−474.
(34) Gharbi, M. A.; Cavallaro, M., Jr; Wu, G.; Beller, D. A.; Kamien, R. D.; Yang, S.; Stebe, K. J. Microbullet assembly: Interactions of oriented dipoles in confined nematic liquid crystal. *Liq. Cryst.* **2013**, *40*, 1619−1627.
(35) Mondiot, F.; Chandran, S. P.; Mondain-Monval, O.; Loudet, J.-C. Shape-induced dispersion of colloids in anisotropic fluids. *Phys. Rev. Lett.* **2009**, *103*, 238303.
(36) Tkalec, U.; Škarabot, M.; Muševič, I. Interactions of micro-rods in a thin layer of a nematic liquid crystal. *Soft Matter* **2008**, *4*, 2402−2409.
(37) Boniello, G.; Luo, Y.; Beller, D. A.; Serra, F.; Stebe, K. J. Colloids in confined liquid crystals: a plot twist in the lock-and-key mechanism. *Soft Matter* **2019**, DOI: 10.1039/C9SM00788A

DOI: 10.1021/acs.langmuir.9b01811
Langmuir 2019, 35, 9274−9285